

**Inelastic muon-proton scattering: Multiplicity distributions and prong cross sections\***

C. del Papa, D. Dorfan, S. M. Flatté, C. A. Heusch, B. Lieberman, G. Luxton,<sup>†</sup> H. Meyer,<sup>‡</sup> L. Moss, T. Schalk, and A. Seiden

*University of California, Santa Cruz, California*

K. Bunnell, M. Duong-van, R. Mozley, A. Odian, F. Villa, and L. C. Wang

*Stanford Linear Accelerator Center, Stanford, California*

(Received 3 February 1976)

In a streamer-chamber experiment at the Stanford Linear Accelerator Center, we observed hadron production in inelastic collisions of 14-GeV positive muons in a liquid hydrogen target. We report on the experiment, the analysis, and the resulting cross sections for hadronic prongs as well as the charged-hadron multiplicity distributions.

**I. INTRODUCTION**

Since the discovery of scaling in inclusive deeply inelastic lepton-nucleon scattering<sup>1</sup> at the Stanford Linear Accelerator Center (SLAC), this process has provided a uniquely promising means of looking at the structure of the nucleon. With this in mind, we undertook a high-statistics experiment, using a specially built streamer-chamber system at SLAC, to look at the full set of charged particles produced in muon-nucleon collisions. In this paper, we present data on topological cross sections and average multiplicities for the production of charged hadrons. We also compare these

quantities with those seen in reactions initiated by other particles.

Our apparatus is shown in Fig. 1. A small-phase-space beam of 14-GeV positive muons was directed onto a 40 cm long, 2.7 cm diameter, cylindrical liquid hydrogen target which was inserted into a large streamer chamber. All beam particles had previously passed through a hole in a  $2.5 \times 2.5 \text{ m}^2$  veto wall of scintillation counters, and entered the transverse field of a large-aperture magnet with a 16 kG field; unless scattered in the target, they then traversed the chamber inside a 5-cm-diameter helium-filled tube. The trigger consisted of a scattered  $\mu^+$  incident on four

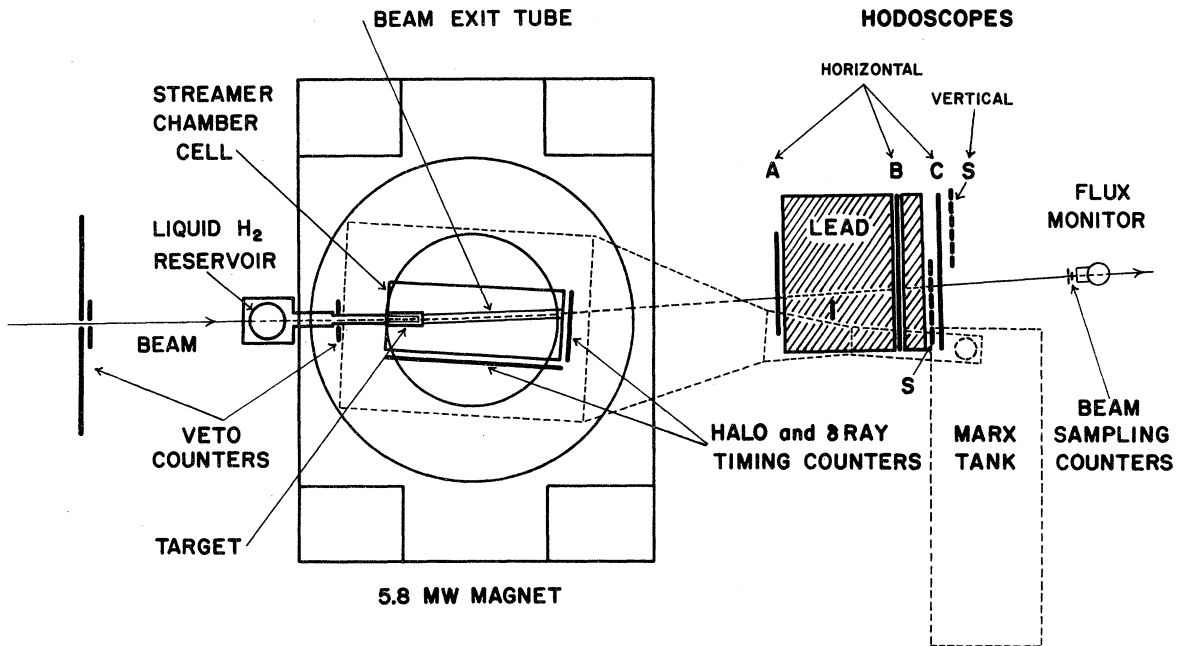


FIG. 1. Plan view of the detection apparatus. The hodoscopes and lead wall had openings for the unscattered beam and the streamer-chamber pulsing system.

banks of scintillator hodoscopes interspersed with 1.5 m of lead.

Charged final-state hadrons produced in the target were detected with nearly complete geometrical acceptance in the streamer chamber, which had an active volume of  $2 \times 0.8 \times 0.6 \text{ m}^3$ . The streamer chamber combines high detection efficiency with electronic triggering. It permits high-statistics investigations even for small cross-section processes; it presently uses photographic means for data acquisition. The effective cross section for our experiment was  $\sim 0.3 \mu\text{b}$ .

In the following sections, we discuss the details of our experimental apparatus, and our methods of analysis. We then report our results on multiplicity distributions for charged hadron production and on topological cross sections. Other features of the data will be discussed elsewhere.

## II. EXPERIMENTAL METHOD

### A. Muon beam

A detailed description of the muon beam, designed and built for this experiment, can be found in Ref. 2. In this paper we focus only on a few major points.

The muons are produced by the primary 20-GeV SLAC electron beam incident on a 2.75-radiation-length high- $Z$  target. Muon production occurs principally via a two-step process. The incident electron radiates a bremsstrahlung photon which subsequently, downstream in the target, produces a muon pair. The short physical size of the target, coupled with the small electron beam size ( $2 \text{ mm} \times 2 \text{ mm}$ ), gives a muon-source size which is very small. The small spot size and the small transverse momentum imparted to the pair-produced muons are the principal advantages for muon-beam production at SLAC as compared to muon beams obtainable at proton accelerators, and they allow the production of a small-phase-space beam with little halo.

The muon-production target is followed by a three-stage beam line whose final focus is at the location of the liquid hydrogen target. Long lead collimators are located at the first two foci for beam definition and momentum selection. To reduce the pion contamination in the beam, it passes through a 3.7-m-long beryllium hadron filter which is located at the first focus of the beam line. The pion contamination in this beam was measured to be  $(4 \pm 1.5) \times 10^{-5}$ .<sup>3</sup>

The final muon beam has a spot size of  $\sigma = 4.2 \text{ mm}$ , an angular divergence of  $\sigma = 2 \text{ mrad}$ , and a momentum bite of  $\sigma = 1\%$ . Halo muons are at a level of 1.6% of the main beam, over the cross-section of the streamer chamber. The intensity

used in the experiment was  $\sim 200$  muons per 1.6- $\mu\text{sec}$ -long SLAC pulse at a muon momentum of 14 GeV/ $c$ . The experiment was typically run at 120 pulses per second, out of a maximum possible 360 that could be delivered by the SLAC machine. The flux limit of the beam line, dictated by power dissipation in the target, is about three times the value used.

### B. Streamer chamber

Figure 2 shows the streamer chamber used to detect charged particles.<sup>4</sup> The chamber consists

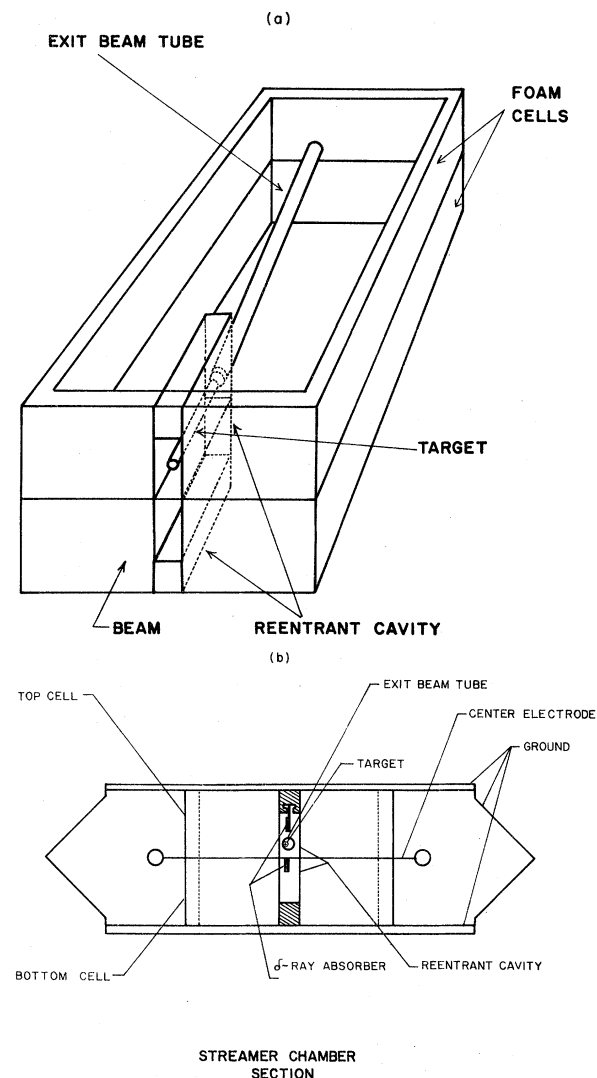


FIG. 2. Perspective and end views of the  $2 \times 0.8 \times 0.6 \text{ m}^3$  streamer chamber. Absorbers above and below the cylindrical target intercept  $\delta$  rays produced in the liquid hydrogen. The helium-filled plastic tube contains the unscattered beams; its walls intercept soft  $\delta$  rays. Electric and magnetic field lines are perpendicular to the midplane.

of two polyurethane foam boxes sandwiched between three electrodes made of stainless steel mesh. The gas used in the chamber is a 90% Ne-10% He mixture. The active chamber volume is 2 m×0.8 m×0.6 m. It is immersed in a 2 m long, 1 m aperture, 16 kG magnet. Both electric and magnetic fields are vertical in direction.

Besides the chamber proper, the streamer-chamber system consists of a triggerable high-voltage source, a Blümlein pulse shaper, and a transmission line section which carries the high-voltage pulse to the chamber.<sup>5</sup> The high voltage is fed onto the mesh electrodes from the downstream end, and terminating resistors connect the voltage planes on the upstream end of the chamber. The system is triggered by a fast-logic muon trigger; up to five triggers per second can be accepted. The high-voltage pulse delivered to the chamber is approximately 500 000 volts maximum amplitude lasting for ~10 nsec.

Every trigger is photographed from above the chamber through the yoke of the magnet by three cameras, with resulting 15° stereoscopy. Numerous fiducials visible just above and below the streamer chamber are simultaneously flashed, and recorded on film for track reconstruction in space.

As seen in Fig. 2, the 40-cm-long liquid hydrogen target is inserted into the upstream end of the chamber. Since the memory time of the chamber is greater than the duration of a SLAC beam pulse, most of the particles passing through the gas in one pulse produce visible tracks. This fact, coupled with the large muon flux per pulse, would be expected to result in the production of a large number of soft  $\delta$  rays (~65 per pulse) by the non-interacting muon beam. Such slow particles would often lead to spiralling tracks, and the resulting ionization density can obscure regions of the chamber on the film. To avoid this effect, we inserted into the chamber a dead region consisting of a reentrant box made of thin Mylar. The box contains the target and is open to the air. This

provides a spark-free region around the liquid hydrogen target, and also allows room for simple target alignment. The box width was chosen to be 9 cm, in order to contain  $\delta$ -ray electrons of energies up to 20 MeV; the number visible in the chamber was thus reduced to a few per pulse. To minimize the number of spirals made by the remaining high-energy  $\delta$  rays, Teflon fins were placed above and below the target to intercept and stop these spiralling particles.

Downstream of the Mylar target box, the beam is contained in a helium-filled Lexan plastic tube. This exit beam tube has a 5 cm diameter and a 1.5 mm wall thickness. This thickness is sufficient to reduce the number of beam-produced  $\delta$  rays in the visible volume of the chamber to a negligible level.

### C. Liquid hydrogen target

The target flask was made of concentric Mylar straws and is shown in Fig. 3. Hydrogen flows into the flask filling the volume of the center straw; it then flows out between this straw and the next concentric one, providing a cold shield. There are thin Mylar caps on each end. The vacuum jacket is formed by a third straw, with its own window; it is glued to a ~1 m long Lexan plastic tube which extends from the target stand into the chamber. Particles produced in the target have to pass through 1.4 mm of Mylar if penetrating normal to the straws, or 0.3 mm of Mylar if passing through the end caps. The target fiducial volume (central straw) is 2.5 cm in diameter, 38.5 cm in length; it contains >98% of the muon beam. The hydrogen feed system used is of the condensation type. The temperature is monitored on both the inflow and outflow lines of the target flask.

### D. Beam-flux monitor

The beam-monitoring system for the experiment consists of a CO<sub>2</sub>-filled total-flux-monitoring Čerenkov (C) counter<sup>6</sup> which intercepts the full

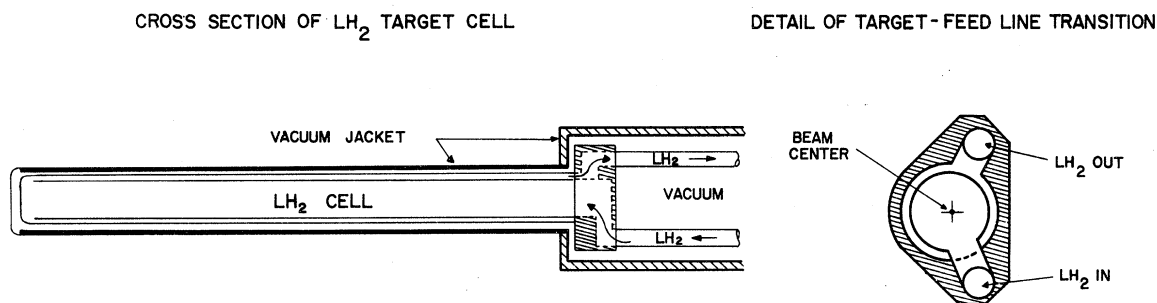


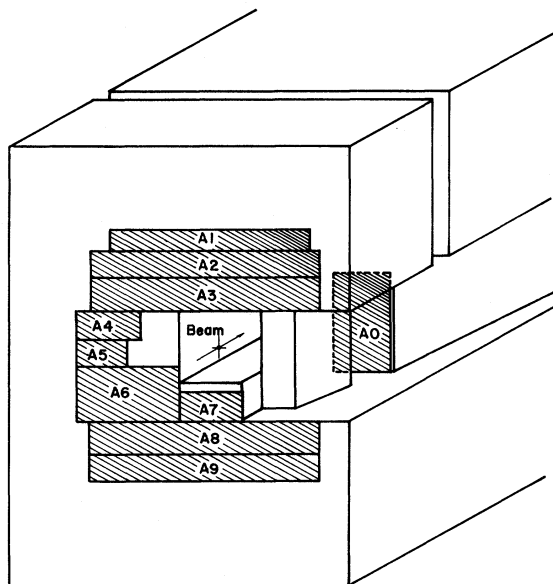
FIG. 3. Liquid hydrogen target and hydrogen flow path.

muon beam, and five small sampling counters to monitor the beam profile. This counter system is shown in Fig. 1.

The gas Čerenkov counter is used as an analog device, gated on and off by the SLAC beam gate. It was initially calibrated at lower muon fluxes by simultaneous counting of individual muons. This calibration is accurate to  $\pm 3\%$  in absolute magnitude. Using small sampling counters, we found the beam profile to be stable to 2 mm in size and location. The central sampling counter is also used to measure electronic dead time; its rate is recorded with and without the experiment veto applied. The dead time for the experiment is generally 20–25% of each beam spill.

#### E. Trigger and veto counters

The muon-trigger counters are arranged in four parallel banks downstream of the streamer chamber. The front bank is horizontal in orientation and located 4.5 m from the beginning of the chamber. It is shown in Fig. 4. This initial bank is directly followed by a 1.5-m-thick lead wall, which has holes for the passage of the beam and for the streamer-chamber voltage feed line. The next two counter banks, also horizontal in orientation, are grouped into narrow coincidences with appropriate counters in the front bank (cf. Fig. 1). The final (fourth) bank is vertical; it is in coincidence as a group with the horizontal counters.



#### A COUNTERS

FIG. 4. Front bank of trigger counters and blocks making up 1.5 m lead wall.

This ensemble of counters forms a rough hodoscope. The coincidence firing a given event provides a region of approximately  $15\text{ cm} \times 20\text{ cm}$ , roughly 5 m from the target through which each trigger-candidate muon must pass. The counter geometry was chosen to give a greater than 60% trigger efficiency for events at  $Q^2 > 1$ , where  $Q^2$  is the negative square of the four-momentum transferred to the hadronic system.

Several meters upstream of the streamer chamber, a large wall of veto counters shadows the trigger system. This wall is about  $2.5 \times 2.5\text{ m}^2$  in area. To further reduce the trigger rate due to the muon halo, small veto counters just upstream of the chamber intercept many of the halo muons that may have slipped through the hole in the large wall. Without the veto counters, the ratio of false triggers to events was about 7000; the veto system reduced it to 12.

#### F. Timing counters

Additional counters are arranged around the periphery of the streamer chamber, as shown in Fig. 1, to provide timing information on forward-produced particles. These counters are used to reject most of the halo muon tracks and high-energy  $\delta$  rays ( $p > 100\text{ MeV}/c$ ) seen in the chamber. These are distributed randomly in time over the beam gate ( $1.6\ \mu\text{sec}$ ) while the timing counters define a  $\sim 20\text{ nsec}$  time interval in coincidence with the muon trigger for acceptance of tracks passing through these counters. Both halo muons and  $\delta$  rays have small angles with respect to the incoming beam and often appear to come from a real event vertex if present in a photograph containing a real event. The number of such halo muons is about 1 per event, the number of such  $\delta$  rays about  $\frac{1}{2}$  per event. Using the timing counters and charge- and momentum-conservation constraints, the number of events in which a  $\delta$  ray or a halo muon is mistakenly accepted as a hadron is less than 1% for each background source.

For each trigger, all the counter information, as well as the roll and frame number of the corresponding chamber photographs, is read into a PDP-9 computer and written onto magnetic tape. In all, 237 000 triggers were recorded. This corresponds to a total flux of  $4.5 \times 10^{10}$  muons.

### III. DATA REDUCTION

#### A. Scanning and measuring

All of the 237 000 frames were doubly scanned for event candidates. Those frames for which scanning information was in disagreement in the first two scans, were rescanned to resolve the conflict. The minimum scanning criterion is one

positive track that is consistent with being a triggering muon, accompanied by at least one other positive track. The efficiency for a single scan was measured to be 98%. The scan selected approximately 44 000 frames. These event candidates were measured on conventional film-plane digitizers which have a least count of 1 micron on film. The setting error for the measurements is 300 microns in space, the demagnification is 67. In order to save measuring time and expedite the results at higher  $Q^2$ , about 50% of the pictures where the trigger indicates a low- $Q^2$  configuration were not measured. This eliminates approximately 24% of the real events, mostly at  $Q^2 \lesssim 0.8$  (GeV/c) $^2$ .

### B. Event reconstruction

The measured events are processed through a three-part reconstruction program: (1) TVGP, the track geometry program which determines the vector momenta for each track; (2) APACHE, a vertex-finding routine which determines the triggering muon using the trigger counter information, reconstructs the primary vertex from the tracks in the event, and recalculates the momentum of each track, using the vertex as the first measured point; and (3) SQUAW, the kinematics fitting program. The momentum accuracy from TVGP is  $\Delta p/p = 1\%$  for a 10 GeV/c track, 2 m long; the mass resolution is illustrated by an 8 MeV FWHM (full width at half maximum) for a  $K^0$  of momentum 2 GeV/c. The vertex errors from APACHE are typically 0.2 mm FWHM transverse to the magnetic field and beam direction, and 1.0 mm along the field or beam. A possible error is the inclusion of a halo (positive) track or a  $\delta$  ray (negative) track in the vertex fit. To eliminate either of these, prior to the vertex fits, all tracks in the event are extrapolated to the timing counters, as discussed earlier. The triggering muon is required to have at least 90 cm of track length visible in the chamber to make its selection and kinematic parameters unambiguous. The reconstruction procedure yielded 10 300 events with a vertex within the target fiducial volume and with at least two positive tracks in the event; one of these is a triggering muon with sufficient visible track length in the chamber. Approximately 2200 of these events are successfully fitted by the elastic scattering hypothesis,  $\mu p \rightarrow \mu p$ .

### C. Data corrections

#### 1. Missing tracks

Although the streamer chamber (Fig. 2) has a large solid-angle acceptance, there are significant

track losses. Since charge conservation requires that in the process of  $\mu^+ p \rightarrow \mu^+ + \text{hadrons}$ , the net charge of the final state be +2, single-track losses are immediately recognized. It is found that in 21% of the events one charged track is lost, in less than 2% two charged tracks are lost. From an analysis of the number of tracks per event, the average probability for a hadron track to be lost is  $(14 \pm 0.5)\%$ . In order to correct for these losses, which are strongly dependent on the angle the secondaries form with the midplane of the chamber, a Monte Carlo rotation program is used. This program rotates the observed events about the beam axis and assigns a weight for each hadron. In addition, a sample of events not balancing charge were carefully rescanned, in a search for anomalies. The results of these investigations

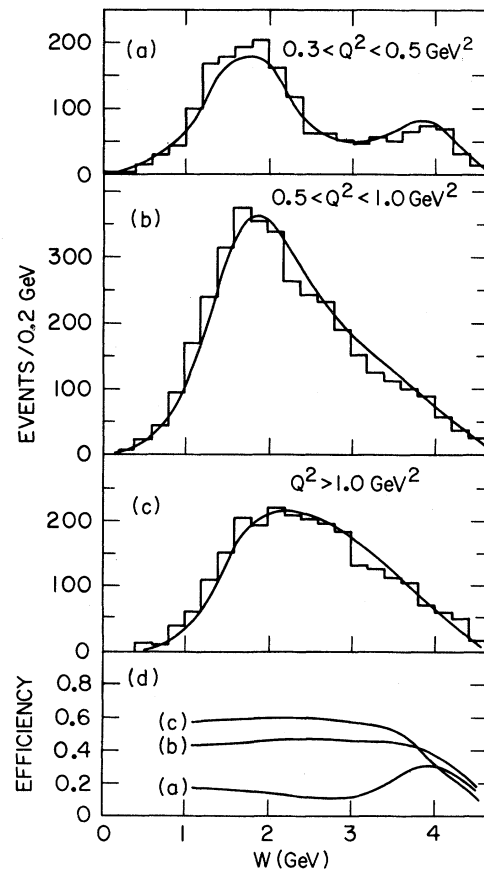


FIG. 5. Observed number of events in our experiment as a function of  $W$  and  $Q^2$ . The events have been weighted for hadron losses in the streamer chamber. Owing to measurement error and beam uncertainty, some events have  $W < m_p$ . The curves are calculated from the known  $ep$  structure functions folded with our geometrical efficiency for muon detection, and are normalized to the total number of observed events over all  $Q^2$  and  $W$ .

are itemized below. For each category, we give an estimated percentage of tracks lost.

(a) The air box surrounding the target extends through the total vertical dimension of the chamber. Tracks having a large "dip angle" can be completely contained within this box. These tracks are therefore invisible, or can be obscured sufficiently to prevent their measurement. Furthermore, steep tracks produce very thick streamers, making measurement imprecise or impossible. There is a resulting loss of 9%.

(b) Hadrons traversing the liquid hydrogen target and the beam exit tube can interact or scatter, and therefore do not reconstruct from the primary vertex. Loss: approximately 2%.

(c) Low-momentum particles may not emerge

into the sensitive chamber due to energy lost in the 2.7-cm-diameter liquid hydrogen target, the target wall, and the air box surrounding the target. This in particular affects protons of  $|p| < 0.2$  GeV/c. Loss: approximately 2%.

(d) The presence of the helium-filled beam-exit tube, which prevents the noninteracting muons from producing copious  $\delta$  rays in the chamber, may hide a high-momentum track from view ( $|p| > 8$  GeV/c for particles produced at  $0^\circ$ ). Loss: approximately 0.5%.

(e) The measurement may erroneously omit a track as a result of the complexity of the event. Loss: approximately 0.5%.

In order to correct for these losses in those events that do not appear to balance charge, the

TABLE I. Fractional prong cross sections for 1, 3, 5, and 7 charged hadrons and average charged hadron multiplicities, vs  $W$ , for three  $Q^2$  intervals. NC: No radiative corrections are applied; RC: values are corrected for radiative effects.

$\langle W \rangle$ (GeV)	$\sigma_1/\sigma_{\text{tot}}$		$\sigma_3/\sigma_{\text{tot}}$		$\sigma_5/\sigma_{\text{tot}}$		$\sigma_7/\sigma_{\text{tot}}$		Mult.		No. of events
	NC	RC	NC	RC	NC	RC	NC	RC	NC	RC	
$0.3 < Q^2 < 0.5 \text{ GeV}^2, \langle Q^2 \rangle = 0.40 \text{ GeV}^2$											
2.5	0.51	0.48 ± 0.08	0.45	0.48 ± 0.08	0.04	0.04 ± 0.02	...	...	2.06	2.13 ± 0.17	61
2.7	0.41	0.39 ± 0.08	0.48	0.50 ± 0.08	0.11	0.12 ± 0.04	...	...	2.39	2.46 ± 0.21	60
2.9	0.31	0.27 ± 0.09	0.61	0.64 ± 0.09	0.08	0.09 ± 0.04	...	...	2.54	2.64 ± 0.21	50
3.1	0.17	0.10 ± 0.07	0.62	0.66 ± 0.09	0.20	0.22 ± 0.07	0.02	0.02 ± 0.02	3.13	3.31 ± 0.22	45
3.3	0.12	0.07 ± 0.06	0.67	0.70 ± 0.08	0.21	0.23 ± 0.06	...	...	3.17	3.31 ± 0.19	55
3.5	0.15	0.09 ± 0.06	0.49	0.52 ± 0.09	0.28	0.30 ± 0.08	0.08	0.09 ± 0.05	3.58	3.77 ± 0.27	51
3.7	0.22	0.16 ± 0.08	0.50	0.54 ± 0.08	0.22	0.24 ± 0.06	0.06	0.07 ± 0.03	3.25	3.43 ± 0.26	62
3.9	0.14	0.06 ± 0.05	0.53	0.58 ± 0.06	0.23	0.26 ± 0.05	0.09	0.10 ± 0.04	3.56	3.81 ± 0.22	93
4.3	0.14	0.0 ± 0.07	0.47	0.53 ± 0.08	0.29	0.35 ± 0.07	0.10	0.12 ± 0.05	3.72	4.18 ± 0.30	88
$0.5 < Q^2 < 1.0 \text{ GeV}^2, \langle Q^2 \rangle = 0.68 \text{ GeV}^2$											
2.1	0.47	0.46 ± 0.03	0.52	0.53 ± 0.03	0.02	0.02 ± 0.01	...	...	2.11	2.13 ± 0.07	313
2.3	0.45	0.43 ± 0.04	0.50	0.51 ± 0.04	0.05	0.06 ± 0.02	...	...	2.22	2.25 ± 0.09	244
2.5	0.40	0.39 ± 0.05	0.47	0.48 ± 0.04	0.13	0.13 ± 0.03	...	...	2.45	2.49 ± 0.12	232
2.7	0.30	0.28 ± 0.04	0.60	0.61 ± 0.04	0.10	0.10 ± 0.02	0.01	0.01 ± 0.01	2.62	2.66 ± 0.11	225
2.9	0.31	0.28 ± 0.04	0.55	0.57 ± 0.04	0.13	0.13 ± 0.03	0.02	0.02 ± 0.01	2.70	2.76 ± 0.12	180
3.1	0.23	0.20 ± 0.04	0.60	0.62 ± 0.05	0.17	0.18 ± 0.03	0.01	0.01 ± 0.01	2.91	3.00 ± 0.12	146
3.3	0.25	0.22 ± 0.05	0.46	0.47 ± 0.05	0.27	0.28 ± 0.05	0.02	0.02 ± 0.02	3.12	3.23 ± 0.18	118
3.5	0.24	0.20 ± 0.08	0.56	0.59 ± 0.07	0.17	0.18 ± 0.04	0.03	0.03 ± 0.02	2.97	3.07 ± 0.22	107
3.7	0.19	0.14 ± 0.05	0.47	0.49 ± 0.06	0.31	0.33 ± 0.06	0.03	0.04 ± 0.02	3.37	3.53 ± 0.19	96
3.9	0.25	0.19 ± 0.06	0.49	0.52 ± 0.06	0.22	0.24 ± 0.05	0.05	0.06 ± 0.02	3.13	3.32 ± 0.21	93
4.3	0.18	0.05 ± 0.07	0.50	0.57 ± 0.07	0.24	0.29 ± 0.05	0.08	0.10 ± 0.03	3.44	3.87 ± 0.26	103
$1.0 < Q^2 < 4.5 \text{ GeV}^2, \langle Q^2 \rangle = 1.75 \text{ GeV}^2$											
2.1	0.50	0.50 ± 0.04	0.46	0.47 ± 0.04	0.04	0.04 ± 0.01	...	...	2.07	2.08 ± 0.08	202
2.3	0.37	0.36 ± 0.04	0.56	0.57 ± 0.04	0.07	0.07 ± 0.02	...	...	2.40	2.42 ± 0.09	196
2.5	0.29	0.28 ± 0.04	0.62	0.63 ± 0.04	0.08	0.08 ± 0.02	0.01	0.01 ± 0.01	2.59	2.62 ± 0.09	192
2.7	0.34	0.32 ± 0.04	0.53	0.54 ± 0.04	0.13	0.13 ± 0.03	...	...	2.60	2.63 ± 0.10	187
2.9	0.26	0.24 ± 0.04	0.55	0.55 ± 0.04	0.20	0.20 ± 0.03	...	...	2.87	2.92 ± 0.11	177
3.1	0.24	0.22 ± 0.05	0.54	0.55 ± 0.05	0.22	0.23 ± 0.05	0.01	0.01 ± 0.01	2.99	3.05 ± 0.17	124
3.3	0.22	0.20 ± 0.04	0.50	0.50 ± 0.05	0.28	0.29 ± 0.05	0.01	0.01 ± 0.01	3.17	3.24 ± 0.15	121
3.5	0.20	0.18 ± 0.04	0.59	0.60 ± 0.05	0.19	0.20 ± 0.04	0.02	0.02 ± 0.01	3.07	3.13 ± 0.14	110
3.7	0.20	0.18 ± 0.05	0.57	0.58 ± 0.07	0.19	0.20 ± 0.05	0.04	0.05 ± 0.02	3.15	3.22 ± 0.16	101
3.9	0.30	0.27 ± 0.06	0.46	0.48 ± 0.06	0.19	0.19 ± 0.05	0.05	0.06 ± 0.03	2.98	3.08 ± 0.22	89
4.3	0.21	0.12 ± 0.06	0.47	0.51 ± 0.06	0.24	0.28 ± 0.06	0.08	0.09 ± 0.03	3.38	3.67 ± 0.22	108

true multiplicity is restored by the addition of one or two units to the observed value. The events with only one hadronic prong, which cannot be corrected in this way, are weighted by the rotation program mentioned earlier. For one-prong events, this correction is typically  $(15 \pm 3)\%$  of the observed one-prong cross section.

### 2. Pion contamination

The rejection against pion triggers provided by the lead shield and the low pion contamination in the beam, both of which were separately measured, resulted in a pion-induced contamination in the final data sample that varied from  $<1\%$  at low  $W$  (=center-of-mass energy of the virtual photon-proton system) to approximately  $6\%$  at high  $W$ . This contamination has a negligible effect on results presented here, so that no correction was applied.

### 3. Radiative corrections

The topological cross sections measured in our experiment must be corrected for radiative effects. We evaluate these corrections by means of a model for  $(\sigma_n/\sigma_{\text{tot}})(Q^2, W)$ . Using this model, we calculate  $T_n^k$ , the number of events in the  $k$ th  $(Q^2, W)$  bin. Radiative corrections,<sup>7</sup> including the tail of the elastic cross section, will change this number to  $S_n^k$ . Thus, if we call our experimentally observed bin population  $N_n^k$ , the radiatively corrected "true" population will be

$$C_n^k = N_n^k - (S_n^k - T_n^k).$$

The model cross sections were obtained from the known  $e-p$  cross section,<sup>9</sup> multiplied by the prong fractions observed in our own data before radiative corrections. They are normalized so that

$$\sum_{n,k} T_n^k = \sum_{n,k} N_n^k.$$

We checked that the final data are not noticeably affected by changes in the model that are of the order of the radiative corrections. Since the error in the radiative correction terms is negligible, we have taken the errors in  $C_n^k$  to be those in  $N_n^k$ . The events are weighted for the muon detection probability, and the error in  $N_n^k$  takes this probability into account.

## IV. RESULTS

### A. Topological cross sections

As an over-all check on our data, a comparison of our observed number of events with a prediction from electron-proton scattering data<sup>9</sup> is shown in Fig. 5. The prediction includes radiative effects, a Monte Carlo simulation of our muon beam and trigger, and the effects of the resolution in measuring the outgoing muon momentum. The agreement is consistent with the uncertainties in the above calculation. We also show our muon trigger efficiency.

The final results of our analysis are presented in Tables I and II; they give explicit details on

TABLE II. Fractional prong cross sections for 1, 3, 5, and 7 charged hadrons, and average charged hadron multiplicities, vs  $Q^2$ , for three  $W$  intervals. NC, RC have the same meaning as in Table I.

$Q^2$ (GeV <sup>2</sup> )	$\sigma_1/\sigma_{\text{tot}}$		$\sigma_3/\sigma_{\text{tot}}$		$\sigma_5/\sigma_{\text{tot}}$		$\sigma_7/\sigma_{\text{tot}}$		Mult.		No. of events
	NC	RC	NC	RC	NC	RC	NC	RC	NC	RC	
2.0 < $W$ < 2.8 GeV, $\langle W \rangle = 2.35$ GeV											
0.5-1.0	0.41	0.40 ± 0.02	0.52	0.53 ± 0.02	0.07	0.07 ± 0.01	...	...	2.32	2.36 ± 0.05	1014
1.0-1.5	0.38	0.37 ± 0.03	0.54	0.55 ± 0.03	0.08	0.08 ± 0.01	...	...	2.39	2.42 ± 0.06	437
1.5-2.0	0.35	0.34 ± 0.04	0.57	0.57 ± 0.04	0.08	0.08 ± 0.02	...	...	2.47	2.49 ± 0.09	178
2.0-4.5	0.39	0.38 ± 0.04	0.54	0.54 ± 0.04	0.07	0.07 ± 0.02	...	...	2.40	2.42 ± 0.10	162
2.8 < $W$ < 3.6 GeV, $\langle W \rangle = 3.17$ GeV											
0.3-0.5	0.19	0.14 ± 0.04	0.60	0.64 ± 0.04	0.19	0.20 ± 0.03	0.02	0.02 ± 0.01	3.07	3.22 ± 0.12	201
0.5-1.0	0.26	0.23 ± 0.03	0.55	0.56 ± 0.03	0.18	0.19 ± 0.02	0.02	0.02 ± 0.01	2.90	2.98 ± 0.08	551
1.0-1.5	0.26	0.24 ± 0.03	0.53	0.55 ± 0.03	0.20	0.21 ± 0.02	0.01	0.01 ± 0.01	2.92	2.99 ± 0.09	292
1.5-2.0	0.19	0.17 ± 0.04	0.61	0.62 ± 0.05	0.20	0.21 ± 0.04	0.01	0.01 ± 0.01	3.05	3.11 ± 0.13	132
2.0-4.5	0.21	0.20 ± 0.04	0.50	0.51 ± 0.06	0.28	0.29 ± 0.05	0.01	0.01 ± 0.01	3.15	3.21 ± 0.16	108
3.6 < $W$ < 4.7 GeV, $\langle W \rangle = 4.04$ GeV											
0.3-0.5	0.16	0.04 ± 0.04	0.50	0.56 ± 0.04	0.25	0.30 ± 0.04	0.09	0.11 ± 0.03	3.54	3.94 ± 0.16	243
0.5-1.0	0.20	0.11 ± 0.04	0.49	0.53 ± 0.04	0.25	0.29 ± 0.03	0.06	0.07 ± 0.02	3.34	3.63 ± 0.14	292
1.0-1.5	0.25	0.20 ± 0.05	0.50	0.53 ± 0.05	0.20	0.22 ± 0.04	0.05	0.05 ± 0.02	3.08	3.24 ± 0.16	158
1.5-2.0	0.18	0.11 ± 0.06	0.46	0.49 ± 0.07	0.30	0.34 ± 0.07	0.06	0.07 ± 0.04	3.48	3.70 ± 0.25	71
2.0-4.5	0.23	0.17 ± 0.07	0.50	0.53 ± 0.08	0.18	0.20 ± 0.06	0.09	0.10 ± 0.04	3.27	3.46 ± 0.27	69

event numbers, fractional cross sections, and average multiplicities for selected  $W$  and  $Q^2$  bins, both before and after the application of radiative corrections. We omitted low- $Q^2$ , low- $W$  data from this compilation, restricting ourselves to a  $Q^2, W$  range where systematic effects on the determination of these quantities are negligible. Note that the number of prongs, for a given topology, refers to hadrons only; the trigger muon is never included.

Figure 6 details the  $Q^2$  dependence of  $\sigma_n/\sigma_{\text{tot}}$  for three different  $W$  bins starting just above the traditional resonance region. Also shown are the values of these quantities in photoproduction ( $Q^2=0$ ).<sup>10</sup> The outstanding features are (1) a lack of any clear dependence on  $Q^2$  for any  $\sigma_n/\sigma_{\text{tot}}$ , *once  $Q^2$  is larger than  $\sim 0.3$* ; (2) sizable systematic differences between the photoproduction values and the  $Q^2 > 0.3$  plateau.

We conclude from this evidence that changes in the individual channels that make up each topology occur in a fashion that leaves the total fractional cross sections approximately unchanged as a function of  $Q^2$ , above  $Q^2=0.3$ . We note a roughly parallel behavior in elastic  $\rho^0$  production,<sup>8</sup> the most prominent identifiable channel in photoproduction. This channel cross section, divided by  $\sigma_{\text{tot}}$ , drops by a factor of about 2.5 in going from  $Q^2=0$  to  $Q^2 \approx 0.3$ , and then changes only by  $\lesssim 20\%$  in the  $Q^2$  range of our experiment.

Figure 7 gives the  $W$  dependence of  $\sigma_n/\sigma_{\text{tot}}$  for  $Q^2 > 1 \text{ GeV}^2$ , together with data from other experiments.<sup>11</sup> All the data shown are in agree-

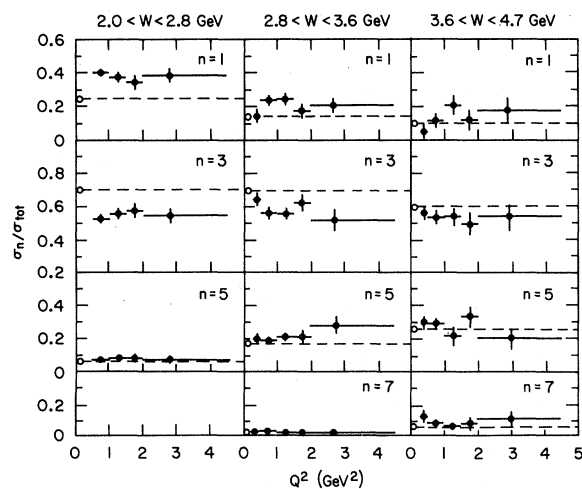


FIG. 6. Fractional topological cross sections as a function of  $Q^2$  for three regions of  $W$ . Radiative corrections have been applied. Photoproduction points for the average  $W$  of the region are given by open circles (Ref. 10).

ment within their statistical and systematic uncertainties. Significant differences from photoproduction exist for 1-, 3-, and 5-prong topologies. In our  $W$  range ( $\sigma_1/\sigma_{\text{tot}}(Q^2 > 0.3)$  is about 50% to 100% larger than ( $\sigma_1/\sigma_{\text{tot}}(Q^2=0)$ ),  $\sigma_3/\sigma_{\text{tot}}$  drops from  $\sim 0.7$  in photoproduction to 0.55, and  $\sigma_5/\sigma_{\text{tot}}$  first rises with  $W$  above the photoproduction value, then falls to a comparable or somewhat smaller value. One might expect that the fall in  $\sigma_3/\sigma_{\text{tot}}$ , and consequent rise in the other channels, is dominated by the decrease of elastic  $\rho^0$  production from 16% of  $\sigma_{\text{tot}}$ .<sup>8</sup> Other possible factors, whose effect cannot be unambiguously determined in this experiment, are the presence of a longitudinal photon component not present in photoproduction, and a possible change (mirroring the elastic case) in inelastic  $\rho^0$  production, which is prominently seen in photoproduction.<sup>12</sup>

### B. Average charged-particle multiplicities

Using the topological cross sections, we can calculate the average number of hadronic prongs (multiplicity) seen. This is shown in Fig. 8, as a function of  $W$ , compared with photoproduction<sup>10</sup> and other experiments.<sup>11</sup> Events with multiplicity greater than 7, of which there were a total of 15, are not included. The effect of this cut on the multiplicity is less than one standard deviation in

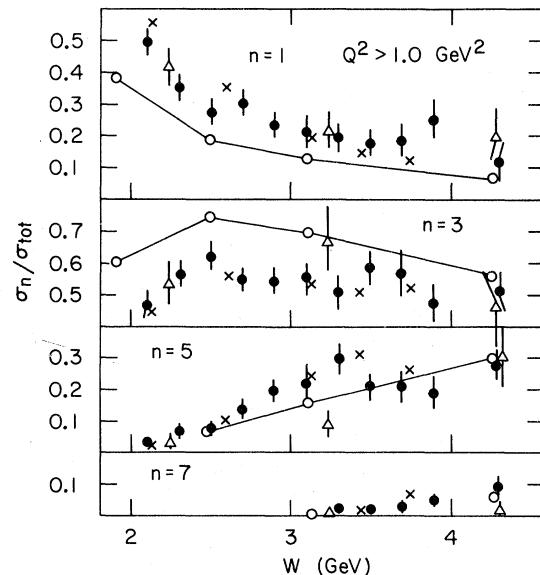


FIG. 7. Fractional topological cross sections as a function of  $W$  for  $Q^2 > 1 \text{ GeV}^2$ . Radiative corrections have been applied. Photoproduction values are shown as open circles which we have connected by a solid line (Ref. 10). The crosses are lepton production data from P. H. Garbincius *et al.*, the triangles from J. Ballam *et al.* (Ref. 11).



all cases. It is seen that the average multiplicity is not too sensitive to the differences seen in the topological cross sections. Only at low  $W$  are the photoproduction values noticeably different (by  $\sim 10\%$ ) from those in deeply inelastic scattering.

In Fig. 9, the average multiplicity is plotted against  $\ln s$  ( $= 2 \ln W$ ), for  $Q^2 > 0.5$ , and compared to the values in  $\pi^- p$  and  $\pi^+ p$  (Ref. 13) scattering. Again, all the various average multiplicities are very close. The  $\pi^- p$  case, which includes zero-prong events, is a little smaller in magnitude;  $\pi^+ p$ , which has  $\geq 2$  prongs, is a little larger.

In purely hadronic reactions, it has been possible to fit the hadronic average multiplicities for  $K^+ p$ ,  $\pi^+ p$ , and  $pp$  reactions, to an accuracy of about 10%, with the same function by using, instead of  $s$ , the variable  $Q = \sqrt{s} - (m_1 + m_2)$ .<sup>14</sup> The masses  $m_1$  and  $m_2$  are those of the initial particles, and the use of  $Q$  instead of  $s$  roughly takes into account the fact that the energies available to create new particles in the various reactions are different because of quantum-number constraints.

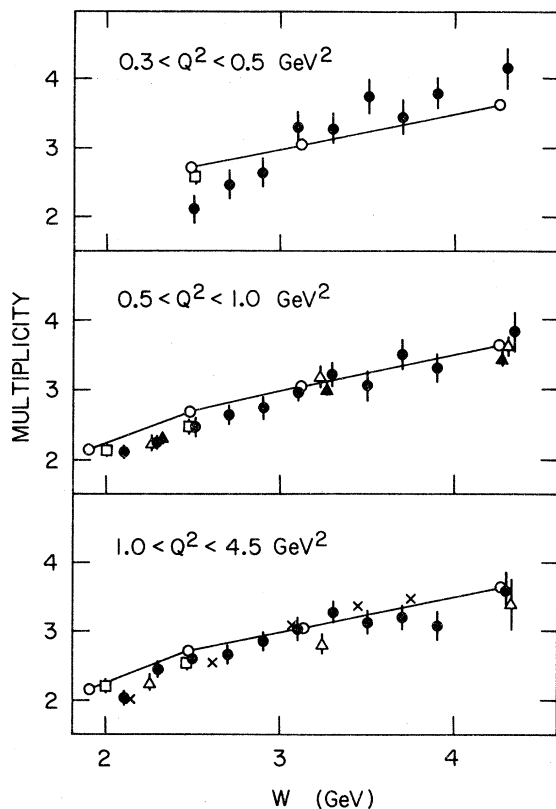


FIG. 8. Average charged multiplicity as a function of  $W$  for three  $Q^2$  regions. Photoproduction values are shown as open circles which we have connected by a solid line (Ref. 10). The crosses are data from P. H. Garbincius *et al.*, the triangles are from J. Ballam *et al.*, the squares are from V. Eckardt *et al.* (Ref. 11).

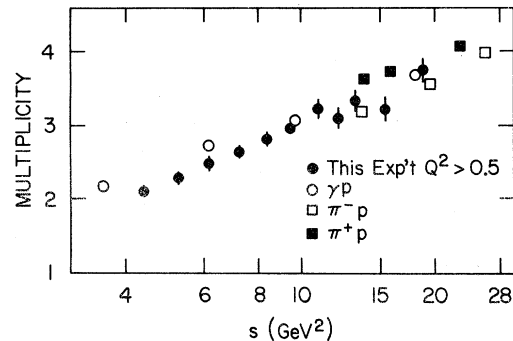


FIG. 9. Multiplicity as a function of  $\ln s$  for  $Q^2 > 0.5$ . Also shown are photoproduction data (Ref. 10) and  $\pi^+ p$  data (Ref. 13).

Figure 9 indicates that the deeply inelastic data, for our  $W$  range, lie roughly on the same universal hadronic multiplicity curve, provided we make the identification  $m_1 + m_2 \approx (m_p + m_\pi)$  (or even  $\approx m_p$ ). This is an interesting result, since it is *a priori* uncertain what mass state is produced in the fragmentation region for photons whose "mass" changes from 0.3 to 4.0, how this state affects the distribution of the available energy, and what the resulting multiplicity may be.

In Fig. 10, we compare  $\langle n \rangle / D$  for the four reactions of Fig. 9, where  $\langle n \rangle$  = mean multiplicity, and  $D = \langle n^2 \rangle - \langle n \rangle^2$  is the dispersion of the multiplicity distribution. For all the hadron reactions mentioned previously, this quantity lies between 2.0 and 2.6 for  $s$  between 15 and 400  $\text{GeV}^2$ . The value near 2.0 has been interpreted as being due to two components—one diffractive, the other multiperi-

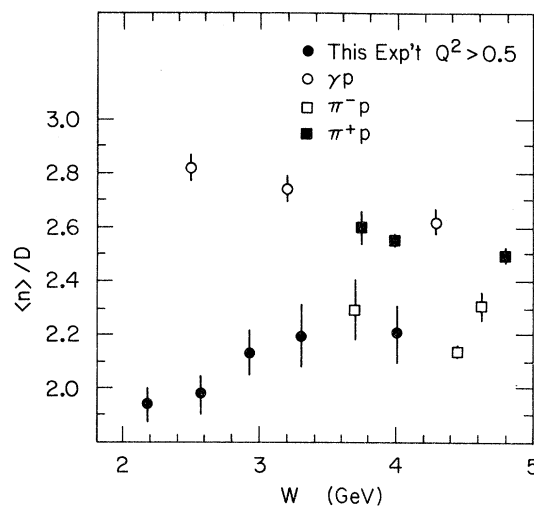


FIG. 10.  $\langle n \rangle / D$  for charged hadron topological cross sections vs  $W$  for  $Q^2 > 0.5$ . The same quantity is shown for photoproduction (Ref. 10) and pion-initiated reactions (Ref. 13).

pheral—contributing to the hadronic cross section.<sup>14, 15</sup> The deeply inelastic cross section is expected to have the diffractive component suppressed, so that the  $\langle n \rangle/D$  value should grow with  $W$ , and be larger than the value seen in hadronic reactions. It is therefore interesting that the  $\langle n \rangle/D$  value for our data is so close to the typical hadronic value. The trend of the  $\langle n \rangle/D$  value is, however, consistent with a growth with  $W$ . A check of this quantity, as well as  $\sigma_n/\sigma_{\text{tot}}$ , at considerably higher values of  $W$  and  $Q^2$  would provide a good

test of the two-component model of hadronic multiplicity distributions.

#### ACKNOWLEDGMENTS

We wish to thank the SLAC operations staff and the engineering and scanning staffs of SLAC and of the University of California at Santa Cruz high-energy group for their invaluable contributions to this work.

---

\*Work supported in part by the U. S. Energy Research and Development Administration.

†Now at Stanford Medical Center, Stanford University, Stanford, California.

‡Visitor from DESY, Deutsches Elektronen-Synchrotron, Hamburg, Germany.

<sup>1</sup>G. Miller *et al.*, Phys. Rev. D **5**, 528 (1972), and earlier references contained therein.

<sup>2</sup>S. M. Flatté, C. A. Heusch, and A. Seiden, Nucl. Instrum. Meth. **119**, 333 (1974).

<sup>3</sup>C. A. Heusch and A. Seiden, Nucl. Instrum. Meth. **124**, 175 (1975).

<sup>4</sup>C. A. Heusch, B. Lieberman, and A. Seiden, Nucl. Instrum. Meth. **124**, 165 (1975).

<sup>5</sup>F. Bulos *et al.*, SLAC Report No. 74 (unpublished).

<sup>6</sup>B. Lieberman, Univ. of California at Santa Cruz Report No. UCSC 71-003 (unpublished).

<sup>7</sup>Radiative-correction code provided by E. Bloom, SLAC (private communication).

<sup>8</sup>See also: C. A. Heusch, in *Proceedings of the XVII International Conference on High Energy Physics, London, 1974*, edited by J. R. Smith (Rutherford High Energy Laboratory, Chilton, Didcot, Berkshire, 1974) p. IV-65; in *Proceedings of the International Confer-*

*ence on High Energy Physics, Palermo, 1975*, edited by A. Zichichi (CERN, Geneva, to be published); R. F. Mozley, in *Proceedings of the 1975 International Symposium on Lepton and Photon Interactions at High Energies, Stanford, California*, edited by W. T. Kirk (SLAC, Stanford, 1976), p. 783.

<sup>9</sup>For the inelastic cross-section we used a phenomenological fit to the MIT-SLAC electroproduction data developed by W. Atwood and S. Stein (private communication).

<sup>10</sup>J. Ballam *et al.*, Phys. Rev. D **5**, 545 (1972); H. H. Bingham *et al.*, *ibid.* **1277** (1973).

<sup>11</sup>P. H. Garbincius *et al.*, Phys. Rev. Lett. **32**, 328 (1974); V. Eckardt *et al.*, Lett. Nuovo Cimento **6**, 551 (1973); J. Ballam *et al.*, Phys. Lett. **56B**, 193 (1975).

<sup>12</sup>E. Kogan, Ph.D. thesis, Weizmann Institute, 1975 (unpublished).

<sup>13</sup>V. V. Ammosov *et al.*, Nucl. Phys. **B58**, 77 (1973).

<sup>14</sup>This is the so-called  $Q$  value, unrelated to the photon "mass"  $Q^2 \equiv -q^2$ ; For a review of present data and relations between different hadron reactions see J. Whitmore, Phys. Rep. **10C**, 273 (1974).

<sup>15</sup>L. Van Hove, Phys. Lett. **43B**, 65 (1973).